Summary of the Advanced Supersonic Parachute Inflation Research Experiment (ASPIRE) Sounding Rocket Tests with a Disk-Gap-Band Parachute

Bryan S. Sonneveldt*, Ian G. Clark†, and Clara O'Farrell‡
Jet Propulsion Laboratory, California Institute of Technology, Pasadena, CA, 91106, USA

Christopher D. Karlgaard§ and Jake A. Tynis¶
Analytical Mechanics Associates Inc., NASA Langley Research Center, Hampton, VA, 23666, USA

I. Introduction

A. ASPIRE Background

Each U.S. robotic mission to the Martian surface to date has used a supersonic Disk-Gap-Band (DGB) parachute to decelerate the spacecraft from supersonic to subsonic speeds as part of the descent and landing sequence. The DGB parachute design used for these missions was developed back in the 1960's and 1970's and used for the first Mars Lander mission, Viking [1]. The development of this parachute consisted of wind tunnel testing [2], [3], [4], low-altitude drop testing [5], and high altitude supersonic parachute testing [6], [7], [8]. After the success of the twin Viking landers, all subsequent NASA Mars landing missions have used a variant of this supersonic DGB parachute design. These missions include Mars Pathfinder (1997) [9], [10], Mars Polar Lander (1999) [11], Mars Exploration Rovers (2004) [12], Phoenix lander (2007) [13], and Mars Science Laboratory (2012) [14]. For each of these missions, the parachute was sized for the given payload and modified in response to technological improvements, but otherwise largely maintained the same characteristics of the original DGB parachute design. Additionally, after Viking, parachute development and qualification testing was limited to subsonic testing via low-altitude drop tests or wind tunnel tests. These tests were generally thought to be structural qualification tests under a hypothesis that the parachute stresses and loads seen during supersonic inflation could be adequately replicated in a subsonic inflation.

In 2014 & 2015 the Low-Density Supersonic Decelerators (LDSD) project tested multiple large aerodynamic decelerator technologies that could be used at Mars including two variants of a 30.5 meter diameter supersonic parachute [15], [16]. While other aerodynamic decelerator technologies performed nominally, the parachutes used in these flight tests failed during inflation [17], [16]. Furthermore, the parachute design that failed in each test had been tested subsonically and shown to survive loads higher than those seen in supersonic flight. This led to a critical need to better understand the dynamics of a supersonic parachute inflation in a Mars-like environment. The Advanced Supersonic Parachute Inflation Research Experiments (ASPIRE) project was formed in order to develop a method of testing full-scale parachutes for Mars at supersonic speeds in conditions that are analogous to those of a Martian entry.

The primary objective of ASPIRE was to act as a risk reduction test activity for the Mars 2020 supersonic parachute [18]. Two candidate parachutes for the Mars 2020 mission were tested across three flights between October 2017 and September 2018. The first candidate parachute was a Build-to-Print version of the Mars Science Laboratory (MSL) parachute built by Pioneer Aerospace. The second parachute was a Strengthened DGB parachute that had the same geometry but differed in materials and construction and was built by Airborne Systems.

ASPIRE used a two stage Terrier-Black Brant IX sounding rocket launched out of Wallops Flight Facility (WFF) in Virginia to deliver these parachutes to Mars-relevant Mach numbers and dynamic pressures. ASPIRE was focused on understanding the inflation process and structurally testing the candidate M2020 parachutes, so each ASPIRE flight targeted a peak inflation load and corresponding dynamic pressure. The first ASPIRE flight, designated SR01, occurred on October 4th, 2017 and carried the MSL Build-to-Print Chute while the second (SR02) and third (SR03) flights tested the Strengthened Parachute design.

*Systems Engineer, Entry Descent and Landing Systems & Advanced Technologies, bryan.s.sonneveldt@jpl.nasa.gov
†Systems Engineer, Entry Descent and Landing Systems & Advanced Technologies
‡Guidance and Control Engineer, Entry Descent and Landing Guidance and Control Systems
§Supervising Engineer, AIAA Senior Member
¶Aerospace Engineer

B. Paper Organization

This paper will present an overview of all three ASPIRE flights. First, the Test Architecture that was used for all three ASPIRE flights will be presented. This will be broken down into an explanation of the Concept of Operations (CONOPS), the parachute test articles, the data sources used, and the process that was used to reconstruct the flight trajectories and parachute performance. Next, the performance and results for all three ASPIRE flights will be presented in the order of the phases of flight. Lastly this paper will discuss the Conclusions and Lessons Learned from those results and from the ASPIRE project as a whole.

II. ASPIRE Test Architecture

Each ASPIRE payload was rail launched atop a 2 stage Terrier-Black Brant IX sounding rocket. Figure 1 shows the length of the vehicle and a breakdown of each payload subsystem. This vehicle and payload configuration was consistent across all three ASPIRE flights.

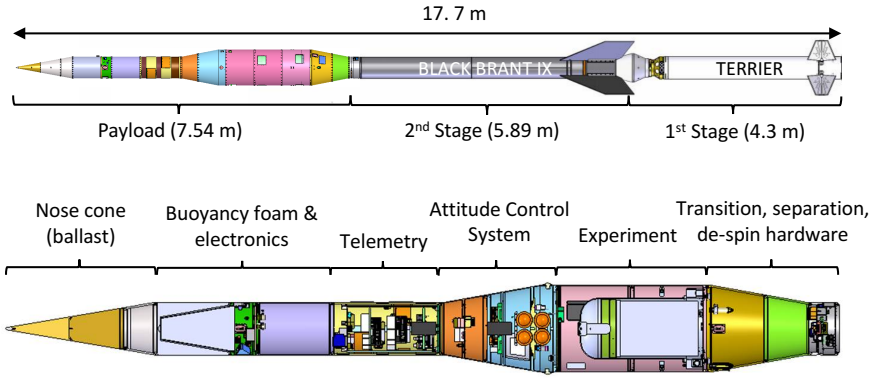

Fig. 1 ASPIRE Payload Configuration

A. CONOPS

Figure 2 shows the Concept of Operations (CONOPS) for all of the ASPIRE flights. The vehicle is rail launched from a 50K launcher on Wallops Island, Virginia. The first stage Terrier motor burns for approximately 4 seconds while the vehicle is spun up for stabilization using spin motors. The second stage Black Brant IX then ignites for a 60 second burn and the vehicle reaches roughly Mach 3.3 at second stage burnout. About 60 seconds later the payload then performs a yo-yo despin maneuver to null the roll rate and separates from the Black Brant. The payload is then in the coast phase where cold gas thrusters of the Attitude Control System (ACS) null any residual rates leading up to parachute deploy. After coasting through an apogee of 45-55 km, the parachute is then mortar deployed when the onboard computer detects the target dynamic pressure condition. Within 2 seconds of mortar fire the parachute is fully inflated and within 6 seconds has decelerated to subsonic speeds. The payload and parachute descend toward the Atlantic Ocean and a larger nosecone ballast separates from the vehicle at an altitude of about 3 km so that the payload will remain buoyant in the water. About 30 minutes from launch, the ASPIRE payload splashes down and a recovery crew recovers both the parachute and payload.

B. Test Article Description

The MSL Build-to-Print Chute is a 21.5 meter nominal diameter DGB parachute made of Nylon, Technora, and Kevlar with a parachute assembly mass of ~58 kg. This parachute design was used successfully for the MSL mission when it landed on the surface of Mars in August of 2012 [14]. The Strengthened parachute has the same geometry but differs in construction and materials. The Strengthened parachute has an assembly mass of ~88 kg.

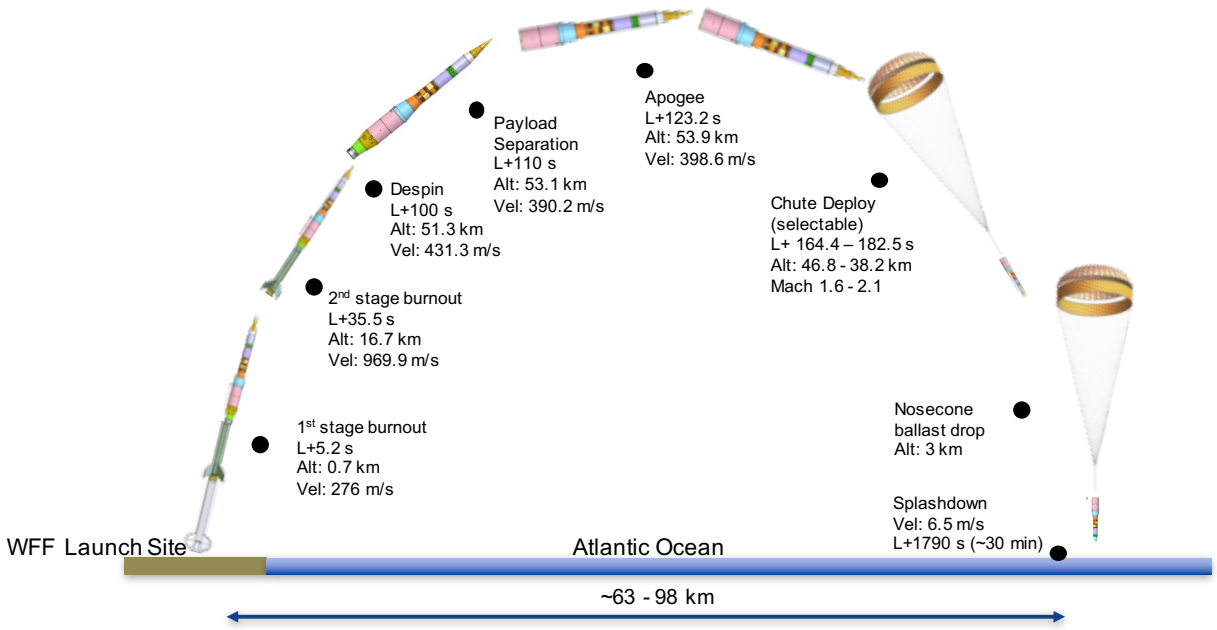

Fig. 2 ASPIRE Concept of Operations

C. Data Sources

1. Test Vehicle Onboard Instrumentation

The ASPIRE payload was equipped with instrumentation to measure the trajectory, aerodynamics, and performance of the test vehicle and test article. Additional instrumentation was used to provide diagnostic information on the payload and its electrical systems, such as temperature or voltage information. A summary of the on-board instrumentation is provided in Table 1.

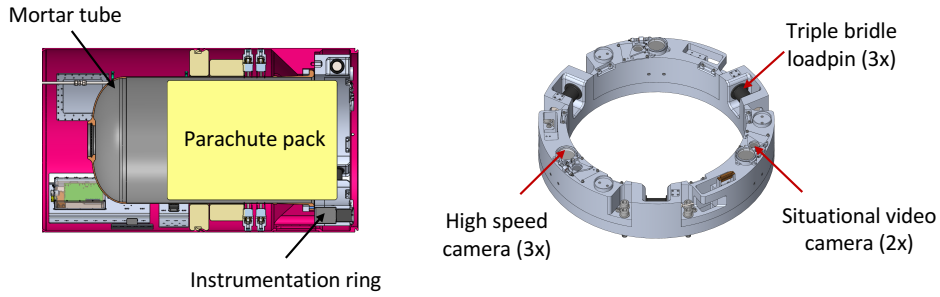

Fig. 3 ASPIRE Instrumentation Ring

2. Range Instrumentation

The test vehicle included a C-band radar beacon with two diametrically opposed antennas located on the section of the payload containing the buoyancy foam (see Figure 1). Multiple fixed radars on the WFF range were used to track the vehicle. One radar was used to track meteorological balloons and the payload first stage motor after separation.

Table 1 Key Instrumentation Summary

Device	Make & Model	Rate	Resolution	Location
Primary IMU	NSROC NIACS	400 Hz	NA	ACS section*
Experimental IMU	NSROC Tern INS	400 Hz	NA	Telemetry section*
GPS	Javad TR-G2	20 Hz	NA	Telemetry section*
Load pins	Strainsert custom	1 kHz	1100 lbf†	Instrumentation ring‡
HS Cameras (x3)	IDT OSX	1000 fps	3840x2400	Instrumentation ring‡
Situational Video (x3)	GoPro Hero4	120 fps	1920x1080	Instrumentation ring‡

* See Figure 1.
‡ See Figure 3 .
† 90 klbf capability, calibrated to 25 klbf on SR01 & SR02 and calibrated to 40 klbf on SR03.

3. Meteorological Instrumentation

Vertical profiles of the atmospheric temperature, pressure, density, and winds spanning from the surface to an altitude of approximately 55 km were derived using a combination of measurements from radiosondes deployed on meteorological balloons and a meteorological analysis from Goddard Spaceflight Center (GSFC).

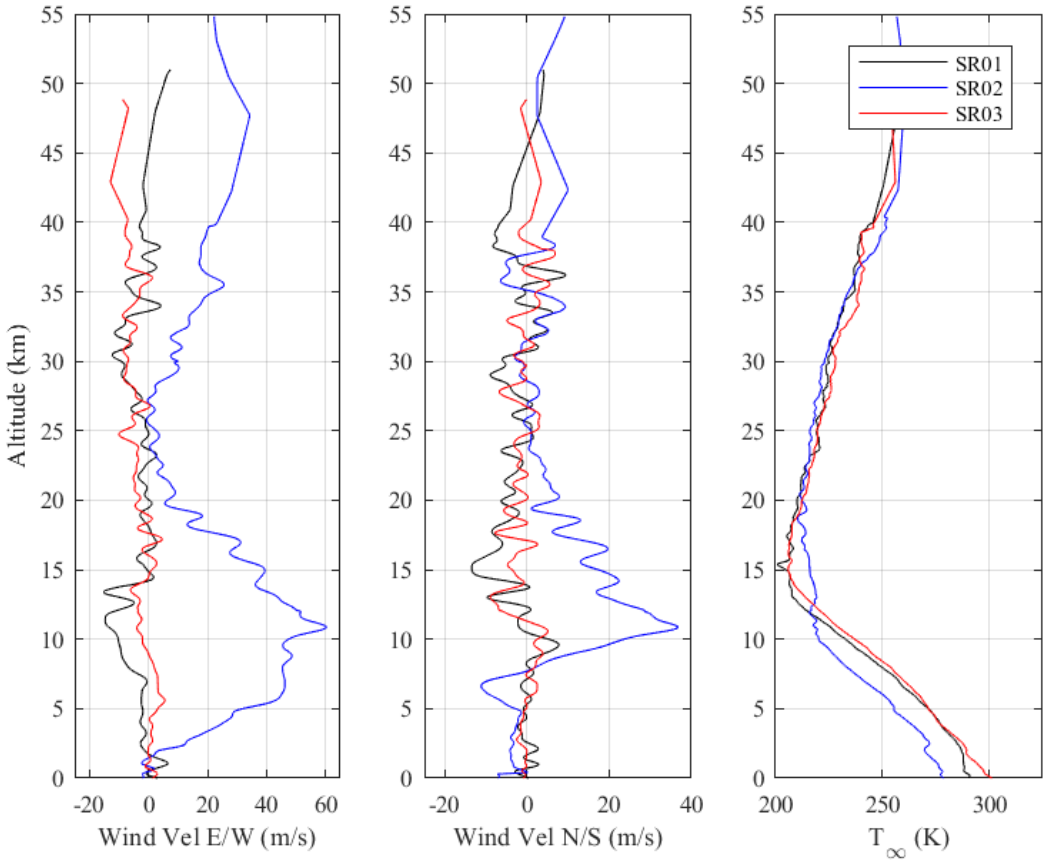

Fig. 4 Atmospheric Profiles

D. Reconstruction Process

After synchronization, the various data sources were incorporated into the reconstruction process. The trajectory of the payload was reconstructed using NewSTEP, a dual-pass Extended Kalman Filter (EKF) developed at NASA LaRC [19]. The filter incorporates the data from the NIACS, GPS, radar, and meteorological instrumentation as well as information about the vehicle configuration to reconstruct the trajectory of the payload from launch until loss of telemetry signal.

III. Flight Results

Tables 2 - 4 show the flight event conditions for all three flights. These tables are to be used as a reference while this section goes through each phase of flight highlighting the important results.

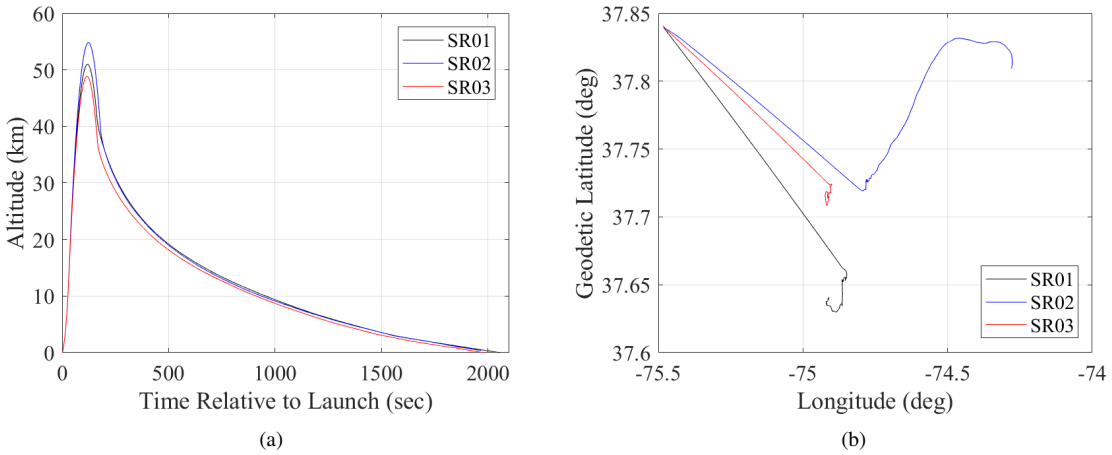

(a) (b)

Fig. 5 ASPIRE Flight Trajectory shown in (*a*) Altitude and (*b*) Latitude vs. Longitude

Table 2 SR01 Event Conditions

Event	T+ *sec*	Mach	Dynamic Pressure *Pa*	WR Velocity *m/s*	Altitude *km*	FPA *deg*	Total AoA *deg*
Launch	0.00	0.01	8.32	3.66	-0.02	35.69	61.66
Brant Burnout	34.27	3.40	89612.93	979.29	15.97	64.13	0.67
Payload Separation	104.03	1.27	87.16	407.80	49.92	20.64	5.92
Apogee	119.05	1.19	65.74	379.66	51.00	0.00	2.11
Mortar Fire	161.41	1.77	452.40	560.29	42.40	-46.40	0.51
Line Stretch	162.37	1.79	491.68	567.74	42.01	-47.05	1.03
Peak Load	162.88	1.77	494.73	560.93	41.80	-47.43	0.87
2nd Peak Load	163.09	1.71	466.32	541.28	41.71	-47.55	2.03
Splashdown	2060.77	0.02	30.50	6.93	-0.01	-51.08	39.61

Table 3 SR02 Event Conditions

Event	T+ *sec*	Mach	Dynamic Pressure *Pa*	WR Velocity *m/s*	Altitude *km*	FPA *deg*	Total AoA *deg*
Launch	0.00	0.02	33.27	7.19	-0.03	5.7	84.89
Brant Burnout	34.10	3.38	82924.79	994.66	16.07	67.3	0.24
Payload Separation	103.99	1.24	53.80	398.06	53.00	28.0	3.83
Apogee	123.49	1.10	33.62	353.25	54.82	0.0	3.03
Mortar Fire	177.59	1.97	670.63	626.75	40.77	-55.8	1.47
Line Stretch	178.63	2.00	744.57	636.42	40.27	-56.2	1.94
Peak Load	179.08	1.97	746.50	626.07	40.03	-56.4	0.60
2nd Peak Load	179.27	1.89	694.69	600.03	39.93	-56.4	5.01
Splashdown	2029.58	0.02	41.37	7.77	0.02	-49.3	45.32

Table 4 SR03 Event Conditions

Event	T+ *sec*	Mach	Dynamic Pressure *Pa*	WR Velocity *m/sec*	Altitude *km*	FPA *deg*	Total AoA *deg*
Launch	0.00	0.03	59.42	10.00	-0.04	-4.97	86.05
Brant Burnout	33.72	3.29	94687.38	946.14	15.33	66.15	0.76
Payload Separation	104.06	1.17	96.41	372.523	48.10	18.70	0.09
Apogee	116.53	1.11	79.36	354.82	48.85	0.00	2.66
Mortar Fire	163.82	1.85	931.71	575.79	38.12	-51.86	0.17
Line Stretch	164.85	1.88	1028.44	584.67	37.65	-52.54	0.90
Peak Load	165.26	1.85	1020.12	573.21	37.45	-52.77	0.48
2nd Peak Load	165.46	1.73	909.60	537.62	37.37	-52.93	1.13
Splashdown	1982.23	0.02	34.99	7.78	0.00	-69.78	22.37

A. Launch

The ASPIRE vehicle launched, exited the rail, and began to spin-up within 1.2 seconds of ignition for each flight. There were no anomalies in the launch process that affected the payload for any of the flights. The separation conditions were a direct result of the performance of the Terrier-Black Brant IX launch vehicle and are shown in Table 5 for a side-by-side comparison.

Table 5 Event Conditions: Payload Separation

Flight	**Time from Launch (sec)**	**Mach**	**Dynamic Pressure (Pa)**	**WR Velocity (m/s)**	**Altitude (km)**	**FPA (deg)**	**Total AoA (deg)**
SR01	104.03	1.27	87.16	407.80	49.916	20.6	5.9
SR02	103.99	1.24	53.80	398.06	52.996	28.0	3.8
SR03	104.06	1.17	96.41	372.53	48.101	18.7	0.1

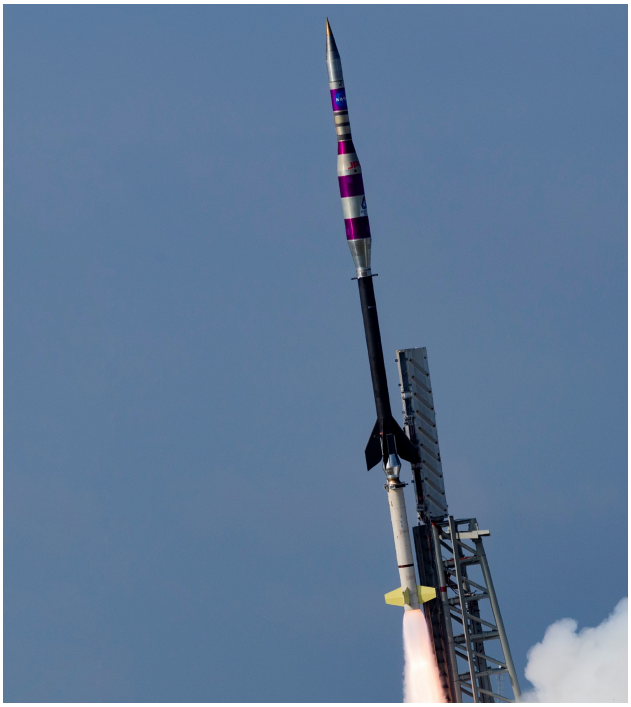

Fig. 6 ASPIRE SR03 Vehicle on the Launch Rail

B. Coast

In the coast phase the Attitude Control System (ACS) of the NIACS performed nominally and kept the payload at a total angle of attack of less than 3 degrees up until mortar fire. Table 6 shows the event conditions at Mortar Fire for each flight. The reconstructed dynamic pressure at trigger was within 6% of the nominal conditions that were targeted for each flight.

Table 6 Event Conditions: Mortar Fire

Flight	Time from Launch (sec)	Mach	Dynamic Pressure (Pa)	WR Velocity (m/s)	Altitude (km)	FPA (deg)	Total AoA (deg)
SR01	161.41	1.77	452.40	560.29	42.40	-46.4	0.51
SR02	177.59	1.97	670.63	626.75	40.77	-55.8	1.47
SR03	163.82	1.85	931.71	575.79	38.12	-51.9	0.17

C. Parachute Deployment and Inflation

On each ASPIRE flight the parachute used the same mortar deploy process that will be used for the Mars 2020 mission. After Mortar Fire (MF) the parachute remains in the parachute bag up until line stretch. Line Stretch (LS) is the time at which the bridles, riser, and suspension lines are fully extended from the payload and the parachute starts to exit the bag and inflate. Bag strip is the process of the parachute emerging from the bag completely. Parachute Full Inflation (FI) is here defined as the first peak load experienced by the parachute.

1. Mortar Fire to Line Stretch

The SR01 parachute bag maintained its orientation almost all the way to line stretch. The SR02 and SR03 parachute bags on the other hand began to rotate soon after exiting the mortar tube and both had rotated at least 90 degrees at line stretch.

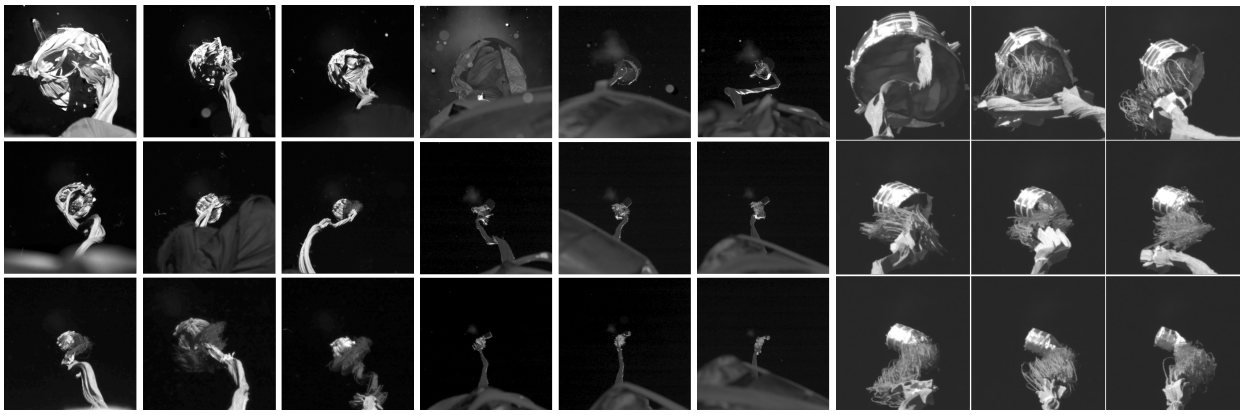

(a) SR01 (b) SR02 (c) SR03

Fig. 7 High Speed Camera Images from Mortar Fire to Line Stretch

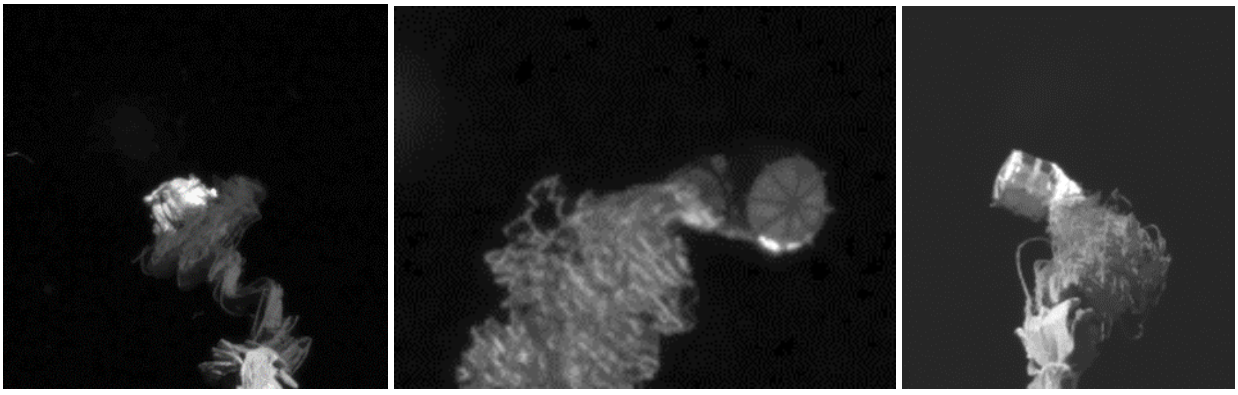

(a) SR01 (b) SR02 (c) SR03

Fig. 8 High Speed Camera Image at Line Stretch

2. Bag Strip

As stated previously, bag strip is the process of the parachute emerging from the bag completely. After the parachute emerges the bag inverts and remains attached to the parachute vent throughout1 the remainder of flight. For all three flights the time from line stretch to bag strip was on the order of 0.25 seconds. On the third flight the parachute bag did not invert in the same manner as on the previous two. On SR03 after the parachute fully emerged the bag did not invert for another 40 milliseconds. Also unique to SR03, the parachute started to inflate before it had fully emerged from the bag. The next subsection will further discuss the differences in the inflation process between flights.

3. Inflation

Figure 11 shows the load trace of the parachute for each flight. The load traces are synchronized at the time of line stretch. Based on this plot it is clear to see how the time from line stretch to full inflation (first peak load) decreases as the flights increased their target peak load and dynamic pressure. Table 7 shows the results from the deploy and inflation process for all three flights.

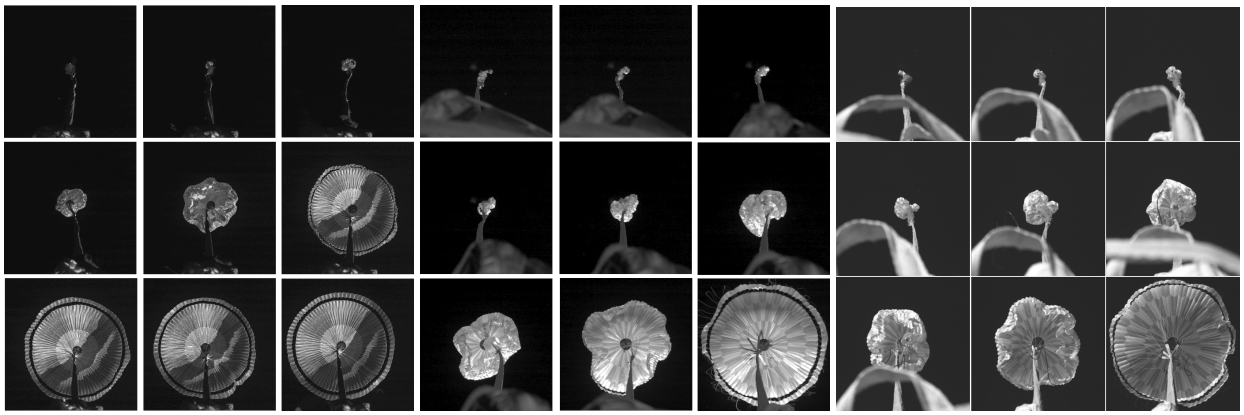

(a) SR01 (b) SR02 (c) SR03

Fig. 9 High Speed Camera Images from Line Stretch to Mortar Fire

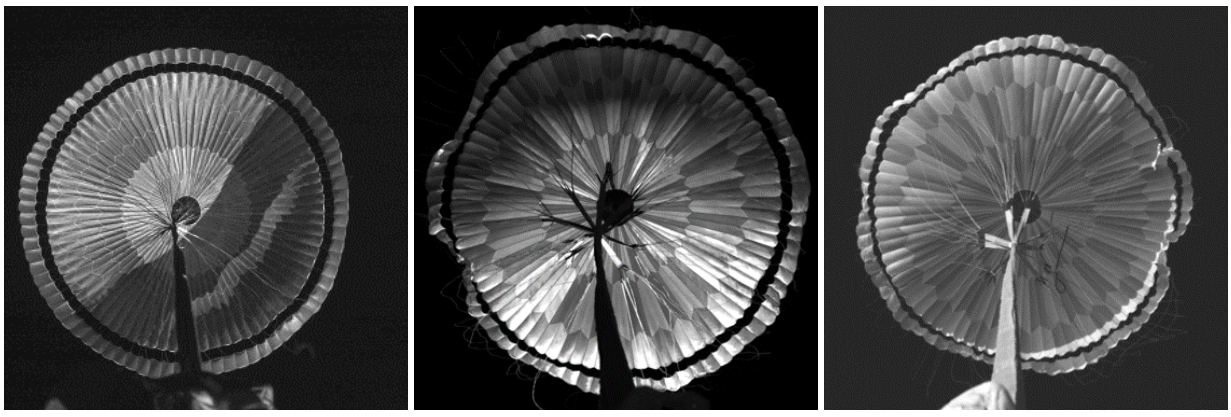

(a) SR01 (b) SR02 (c) SR03

Fig. 10 High Speed Camera Image at Full Inflation

Table 7 Parachute Inflation Results

Parameter	Units	SR01	SR02	SR03
Time from MF to LS	sec	0.96	1.037	1.027
Time from MF to FI	sec	1.467	1.492	1.437
F_{chute} @ Full Inflation	lbf	32,387	50,521	67,336
F_{chute} @ 2nd peak	lbf	32,336	55,982	66,515
q_∞ @ Full Inflation	Pa	494.73	746.5	1020.03
Mach @ Full Inflation		1.77	1.97	1.85
S_0	m^2	356.66	363.16	364.62
S_{proj} @ Full Inflation	m^2	190.16	192.75	193

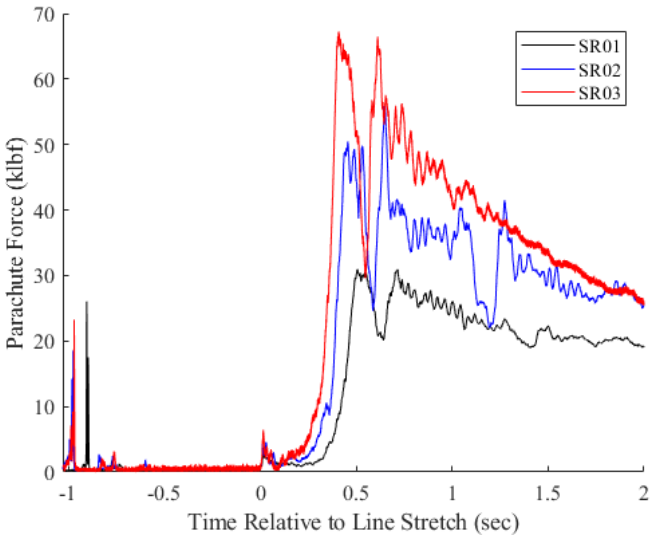

Fig. 11 Parachute Force during Inflation

D. Parachute and Payload Descent

1. Parachute Drag Coefficient

The coefficient of drag of the parachute was calculated using both the load pins and the accelerations from the IMU of the NIACS. Figure 12 shows the results of both calculation methods. The lightly shaded regions in these plots is the 3σ uncertainty in C_D. The uncertainty in the load pin calculation is much greater at lower C_D values because the load pin signal amplifiers were tuned specifically for the peak load event.

Using the load pin data and the reconstructed trajectory the coefficient of drag of the parachute was also mapped with the Mach number for each flight. The results showed that the C_D vs. Mach for each flight was remarkably similar.

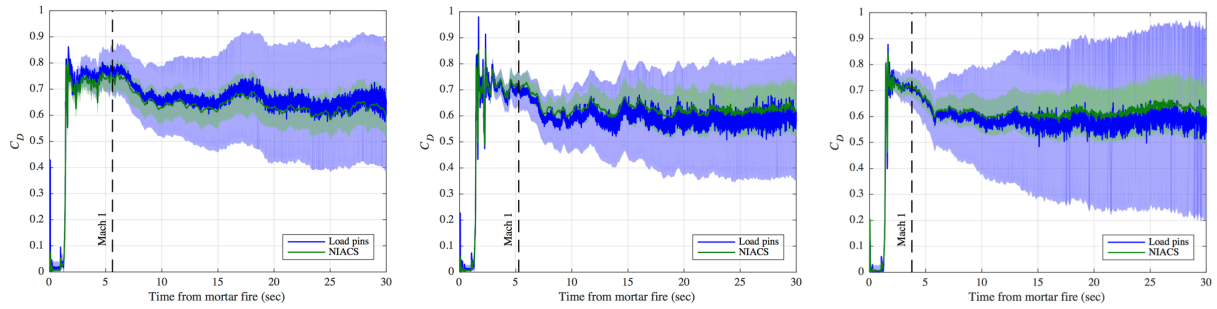

(a) SR01 (b) SR02 (c) SR03

Fig. 12 Coefficient of Drag after Mortar Fire for each flight

2. Parachute Pull Angle

Figure 13 shows a projection of the parachute force vector onto the parachute skirt plane for the first 20 seconds after Mortar Fire. This position was calculated using data from the parachute bridle load pins. It is obvious to see that the parachute position was much more dynamic on SR02 compared to the other flights. There are multiple factors that may have led to this increased level of activity but the true cause is unclear. The wind relative total angle of attack of the payload just prior to line stretch was ~2 degrees on SR02 and only ~1 degree on SR01 and SR03. The Mach number at line stretch and inflation was also higher on SR02 compared to the other flights by 0.1 (see Tables 2 - 4). Currently, the activity seen in Fig. 13 cannot be attributed to one single factor with certainty.

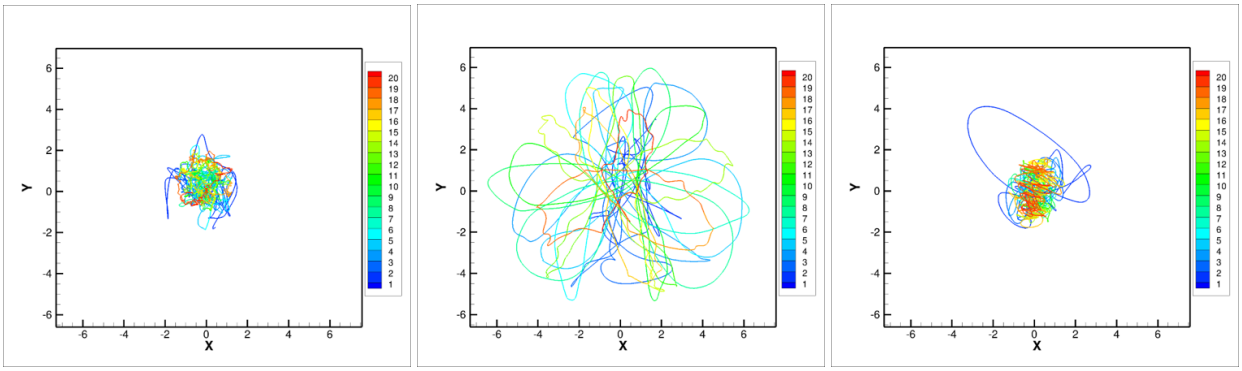

(a) SR01 (b) SR02 (c) SR03

Fig. 13 Parachute Position relative to payload centerline (meters) from Mortar Fire to 20 seconds after Mortar Fire. The color bar shows seconds relative to Mortar Fire

3. Payload Attitude and Rates

Figure 14 and 15 show the wind relative total angle of attack and the roll rate of the payload for the first 100 seconds after Mortar Fire. In both of these plots the SR02 flight shows much more dynamic behavior for the first ~15 seconds. After the 15 second mark all three flights show similar oscillatory behavior but with a higher amplitude for both total angle of attack and roll rate on SR02.

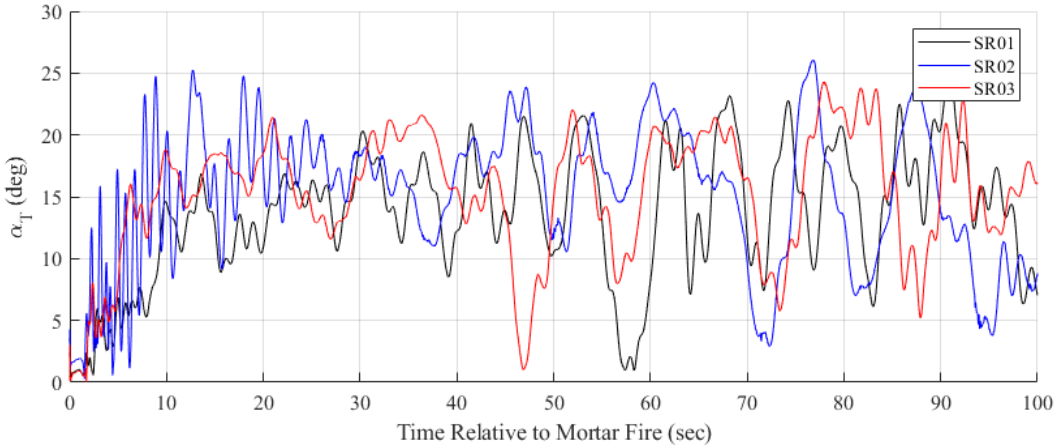

Fig. 14 Payload Total Angle of Attack after Mortar Fire

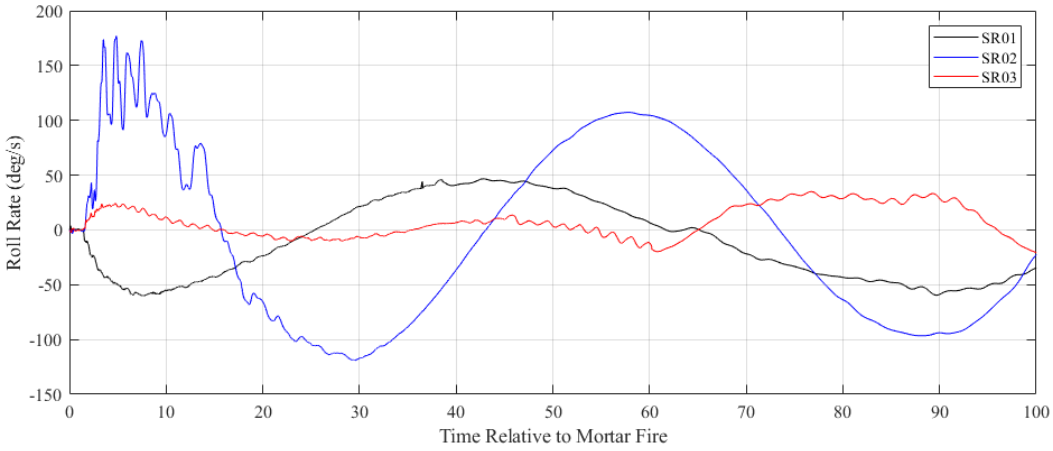

Fig. 15 Payload Roll Rate after Mortar Fire

E. Recovery

For the first and last ASPIRE flights (SR01 & SR03) the recovery crew was able to spot the payload and witness splashdown from about 100 yards away. On these flights the parachute was recovered successfully within 7 minutes after splashdown. On the day of the SR02 flight the sea state was more dynamic than it was for the others, and this made it difficult to cover ground in a short period of time. Due to these conditions the recovery boat did not reach the payload and parachute until 45 minutes after splashdown and both were not fully on board the recovery vessel until 90 minutes after splashdown.

F. Parachute Inspection

After each ASPIRE flight the parachute was rinsed free of salt water then hung up to dry for a few days before being shipped out to US Naval Weapons Center China Lake in order to be inspected. On each flight there was minor damage found in the parachute that was likely related to the deployment process. This led to minor changes in the parachute bag and attachments from the parachute to the bag between flights. The inspections did not find any significant damage to the broadcloth from inflation and found no recovery-induced damage.

(a) SR01 (b) SR02 (c) SR03

Fig. 16 Recovery Vessel Arriving at Payload and Parachute after Splashdown

IV. Conclusions and Lessons Learned

Across all three ASPIRE flights both candidate parachutes performed nominally. Despite the varying activity observed between the three flights, such as the dynamic movement of the parachute in SR02 or the parachute inflating out of its bag on SR03, the parachutes withstood the stresses of deployment and inflation without significant damage. On SR03 the Strengthened chute even experienced a load that is 40% higher than the highest load expected for the Mars 2020 mission.

The ASPIRE project also successfully developed an architecture that can be used to test full scale parachutes for Mars landing missions. The ability to replicate the conditions for a parachute inflation at Mars has proven invaluable.

One area of interest from the ASPIRE results was the unique parachute dynamics seen in the SR02 flight. The movement of the parachute was much greater than the other flights and the maximum load on the parachute was experienced in the second peak instead of the first. As stated before, it is difficult to pinpoint root cause for this unique behavior, but there were a few key factors that could have played a part. One of these factors was the payload angle of attack and rates leading up to line stretch on SR02. Another was the higher Mach number at line stretch and full inflation on SR02. While some of this behavior showed up in the pre-flight simulations, one takeaway was that parachutes and soft goods are very difficult to predict. It would most likely require more test flights to be able to pinpoint the cause and repeatability of these dynamics.

There were also many lessons learned about both the limitations and the drivers for a test architecture like this one. Those lessons were in the targeting process, the limitations in atmospheric measurements, the limitations when measuring loads on a parachute as high as was seen on ASPIRE, and the recovery process.

Acknowledgments

This research was carried out at the Jet Propulsion Laboratory, California Institute of Technology, under contract with the National Aeronautics and Space Administration. The authors would like to gratefully acknowledge the many contributions of the members of the ASPIRE team from Wallops Flight Facility, NASA Langley Research Center, NASA Ames Research Center, and Jet Propulsion Laboratory.

References

[1] Cooley, C. G., and Lewis, J. G., "Viking 75 Project: Viking, Lander System Primary Mission Performance Report," *NASA Contractor Report*, , No. CR-145148, Apr 1977, p. 118.

[2] Galigher, L. L., "Aerodynamic Characteristics of Ballutes and Disk-Gap-Band Parachutes at Mach Numbers From 1.8 to 3.7," *AEDC Technical Report*, , No. AEDC-TR-69-245, 1969.

[3] Bobbitt, P. J., J, M. R., L, F. G., and L, G. L., "Supersonic and Subsonic Wind-Tunnel Tests of Reefed and Unreefed Disk-Gap-Band Parachutes," *AIAA Paper*, , No. 1970-1172, 1970.

[4] Jaremenko, L., S, S., and Faye-Petersen, R., "Scale Model Test Results of the Viking Parachute System at Mach Numbers from 0.1 Through 2.6," *NASA Contractor Report*, , No. CR-149377, 1971.

[5] Eckstrom, C. V., and Murrow, H. N., "Flight Tests of Cross, Modified Ringsail, and Disk-Gap-Band Parachutes from a Deployment Altitude of 3.05 km (10,000 ft)," *NASA Technical Memorandum*, , No. TM X-2221, June 1971.

[6] Eckstrom, C. V., and Preisser, J. S., "Flight Test of a 30-Foot-Nominal-Diameter Disk-Gap-Band Parachute Deployed at a Mach Number of 1.56 and a Dynamic Pressure of 11.4 Pounds Per Square Foot," *NASA Technical Memorandum*, , No. TM X-1451, Aug 1967.

[7] Preisser, J. S., and Eckstrom, C. V., "Flight Test of a 40-Foot-Nominal-Diameter Disk-Gap-Band Parachute Deployed at a Mach Number of 1.91 and a Dynamic Pressure of 11.6 Pounds Per Square Foot," *NASA Technical Memorandum*, , No. TM X-1575, Aug 1968.

[8] Preisser, J. S., and Eckstrom, C. V., "High Altitude Flight Test of a Reefed 12.2-Meter Diameter Disk-Gap-Band Parachute With Deployment at a Mach Number of 2.58," *NASA Technical Memorandum*, , No. TN D-6469, Aug 1971.

[9] Fallon, E. J., "System Design Overview of the Mars Pathfinder Parachute Decelerator Subsystem," *AIAA Paper*, , No. 1997-1511, 1997.

[10] Spencer, D. A., Blanchard, R., Braun, R. D., Kallemeyn, P. H., and Thurman, S. W., "Mars Pathfinder Entry, Descent, and Landing Reconstruction," *Journal of Spacecraft and Rockets*, Vol. 36, No. 3, 1999, pp. 357–365.

[11] Cruz, J. R., and Lingard, J. S., "Aerodynamic Decelerators for Planetary Exploration: Past, Present, and Future," *Tech. Rep.*, , No. 2006-6792, 2006.

[12] Witkowski, A., and Bruno, R., "Mars Exploration Rover Parachute Decelerator System Program Overview," *AIAA Paper*, , No. 2003-2100, 2003.

[13] Adams, D. S., Witkowski, A., and Kandis, M., "Phoenix Mars Scout Parachute Flight Behavior and Observations," *IEEE Aerospace Conference Paper*, , No. 1534, 2011.

[14] Cruz, J. R., Way, D. W., Shidner, J. D., Davis, J. L., Adams, D. S., and Kipp, D. S., "Reconstruction of the Mars Science Laboratory Performance and Comparison to the Descent Simulation," *AIAA Paper*, , No. 2013-1250, 2013.

[15] Gallon, J., Witkowski, A., Clark, I. G., Rivellini, T., and Adams, D. S., "Low Density Supersonic Decelerator Parachute Decelerator System," *AIAA Aerodynamic Decelerator Systems (ADS) Conference*, 2013, p. 1329.

[16] Clark, I., and Adler, M., "Summary of the second high-altitude, supersonic flight dynamics test for the LDSD project," *2016 IEEE Aerospace Conference*, 2016, pp. 1–24. doi:10.1109/AERO.2016.7500618.

[17] Clark, I. G., Manning, R., and Adler, M., "Summary of the First High-Altitude, Supersonic Flight Dynamics Test for the Low-Density Supersonic Decelerator Project," *23rd AIAA Aerodynamic Decelerator Systems Technology Conference*, 2015.

[18] Tanner, C. L., Clark, I. G., and Chen, A., "Overview of the Mars 2020 Parachute Risk Reduction Plan," *Tech. Rep.*, 2018.

[19] Karlgaard, C., Tartabini, P., Martin, J., Blanchard, R., Kirsch, M., and Thornblom, M., "Statistical Estimation Methods for Trajectory Reconstruction: Application to Hyper-X," Tech. Rep. TM-200-215792, 2009.

